AJNR

Experimental Study of Intracranial Hematoma Detection with Flat Panel Detector C-Arm CT

H. Arakawa, M.P. Marks, H.M. Do, D.M. Bouley, N. Strobel, T. Moore and R. Fahrig

AJNR Am J Neuroradiol 2008, 29 (4) 766-772
doi: https://doi.org/10.3174/ajnr.A0898
http://www.ajnr.org/content/29/4/766

ORIGINAL RESEARCH

Experimental Study of Intracranial Hematoma Detection with Flat Panel Detector C-Arm CT

H. Arakawa
M.P. Marks
H.M. Do
D.M. Bouley
N. Strobel
T. Moore
R. Fahrig

BACKGROUND AND PURPOSE: Intracranial hemorrhage is a commonly acknowledged complication of interventional neuroradiology procedures, and the ability to image hemorrhage at the time of the procedure would be very beneficial. A new C-arm system with 3D functionality extends the capability of C-arm imaging to include soft-tissue applications by facilitating the detection of low-contrast objects. We evaluated its ability to detect small intracranial hematomas in a swine model.

MATERIALS AND METHODS: Intracranial hematomas were created in 7 swine by autologous blood injection of various hematocrits (19%–37%) and volumes (1.5–5 mL). Four animals received intravascular contrast before obtaining autologous blood (group 1), and 3 did not (group 2). We scanned each animal by using the C-arm CT system, acquiring more than 500 images during a 20-second rotation through more than 200°. Multiplanar reformatted images with isotropic resolution were reconstructed on the workstation by using product truncation, scatter, beam-hardening, and ring-artifact correction algorithms. The brains were harvested and sliced for hematoma measurement and compared with imaging findings.

RESULTS: Five intracranial hematomas were created in group 1 animals, and all were visualized. Six were created in group 2, and 3 were visualized. One nonvisualized hematoma was not confirmed at necropsy. All the others in both groups were confirmed. In group 1 (with contrast), small hematomas were detectable even when the hematocrit was 19%–20%. In group 2 (without contrast) C-arm CT was able to detect small hematomas (<1.0 cm^2) created with hematocrits of 29%–37%. The area of hematoma measured from the C-arm CT data was, on average, within 15% of the area measured from harvested brain.

CONCLUSIONS: The image quality obtained with this implementation of C-arm CT was sufficient to detect experimentally created small intracranial hematomas. This capability should provide earlier detection of hemorrhagic complications that may occur during neurointerventional procedures.

Neuroendovascular treatment by using fluoroscopy is now playing increasingly important roles in the treatment of ischemic and hemorrhagic lesions in the cerebrovascular circulation; and hardware development, including digital subtraction angiography and rotational angiography, has contributed to this advancement. Intracranial hemorrhage is a widely recognized complication of these procedures, producing lesions with low contrast relative to background tissue signal intensity. Earlier recognition and management of such complications can improve clinical outcomes. Unfortunately, currently available fluoroscopic imaging techniques do not depict such lesions, and transportation of the patient from the interventional suite to a CT scanner is usually required to confirm their presence or absence. Recently, a new fluoroscopy system (AXIOM Artis dTA; Siemens Medical Solutions, Forchheim, Germany) that is also capable of producing low-contrast CT images has been developed, which may permit visualization of such lesions in the cath lab, thereby reducing time to critical decision-making as well as reducing risks to the patient from the transport itself.[1,2]

The new fluoroscopy system consists of a C-arm-mounted flat panel that rotates up to 220° in 4–20 seconds, depending on the protocol, acquiring more than 500 projection images, which can be reconstructed to provide 3D C-arm CT images. The volume images when displayed as multiplanar reconstructions (MPR) facilitate detection of low-contrast objects and provide the ability to obtain 3D soft-tissue information during neuroendovascular procedures.

The size of hemorrhagic lesion that can be detected and the ability to detect such a hemorrhage in a hyperacute timeframe are still open questions. In this study, we assessed the ability of the flat panel detector (FPD) system to image small hyperacute intracranial hematoma (ICH) as a higher attenuation mass within a brain by using a pig ICH model.

Materials and Methods

Animal Model

A total of 8 specific pathogen-free Yorkshire pigs weighing 20–40 kg were obtained from a local vendor. All animals received humane compassionate care, and all procedures in the protocol were approved by the Administrative Panel on Laboratory Animal Care of the university.

All swine fasted overnight and were premedicated with tiletamine and tiletamine/zolazepam (Telazol). Animals were placed on the angiography table, and general anesthesia was induced with gas-inhalant isoflurane by face mask and maintained with isoflurane via endotracheal intubation. A 6–8F femoral artery line was started with a vascular sheath by regular Seldinger technique (percutaneous puncture) to monitor continuously invasive blood pressures as well as draw multiple blood samples to access arterial blood gas values and activated clotting times. This arterial line was continuously flushed

Received July 27, 2007; accepted after revision October 12.

From the Departments of Radiology (H.A., M.P.M., H.M.D., N.S., T.M., R.F.), Comparative Medicine (D.M.B.), and Neurosurgery (M.P.M., H.M.D.), Stanford University Medical Center, Stanford, Calif; and Siemens Medical Solutions (N.S., T.M.), Erlangen, Germany.

This work was supported by NIH EB003524, Siemens Medical Solutions, and the Lucas Foundation.

Please address correspondence to: Michael P. Marks, MD, Department of Radiology, Stanford University Medical Center, 300 Pasteur Dr, Stanford, CA 94305-5105; e-mail: mmarks@stanford.edu

DOI 10.3174/ajnr.A0898

Table 1: Summary of injected blood and results of group 1

Animal No.	Side	Injected Volume (mL)	Hct (%)	ACT (Second)	Area from FPD (cm^2)	Area from Necropsy Brain (cm^2)	Difference (% difference)
1	Rt	5	24	140	0.79	0.79	0.00 (0.0)
	Lt	Not injected					
2	Rt	2.5	26	140	0.56	0.52	0.04 (7.7)
	Lt	Not injected					
3	Rt	2.5	26	113	0.14	0.18	0.04 (22.2)
	Lt*	Not injected			0.22	0.20	0.02 (10.0)
4	Rt	2.5	19	118	0.22	0.17	0.05 (29.4)
	Lt	1.5	20	N/A	0.31	0.30	0.01 (3.3)

Note:—Hct indicates hematocrit; ACT, activated clotting time; FPD, flat panel detector; Rt, right; Lt, left; N/A, not available.
*Hematoma was formed due to ventricular rupture associated with hematoma creation within the right hemisphere; area measured reflected only the hematoma, not the IVH.

Table 2: Summary of injected blood and results of group 2

Animal No.	Side	Injected Volume (mL)	Hct (%)	ACT (second)	Area from FPD CT (cm^2)	Area from Necropsy Brain (cm^2)	Difference (% difference)
5	Rt	10	21	102	Nonvis	0.46	N/A
	Lt	5	22	115	Nonvis	0.41	N/A
6	Rt	5	37	87	0.77	0.71	0.06 (8.5)
	Lt	5	31	70	Nonvis	N/A	N/A
7	Rt	5	29	146	0.55	0.58	0.03 (5.2)
	Lt	5	35	59	0.17	0.13	0.04 (30.8)

Note:—Hct indicates hematocrit; ACT, activated clotting time; FPD, flat panel detector; Nonvis, nonvisible; Rt, right; Lt, left; N/A, not available.

with a 1% heparinized saline throughout the procedure. In addition, an 8F red rubber tube was manually placed through the urethra to gain access to the urinary bladder, thereby allowing accurate recording of urinary output. Renal function was assessed by the appearance of urine concentration or dilution and observation for hematuria, as well as volume produced. With the increased use of contrast (diuretic), a natural body response was increased urinary output. The volume excreted by the pig was closely matched to the volume of warmed lactated Ringer or 0.9% sodium chloride fluids administered via intravenous catheter or through the venous sheath preplaced in the femoral vessel for a larger bolus of fluids. Blood pressure was continuously monitored and evaluated to prevent hypovolemia or fluid overload. Arterial blood gas sampling at 30-minute intervals permitted adjustments in anesthesia/ventilation/fluid therapy, keeping the animal stable and in a state of homeostasis.

Seven swine were divided into 2 groups. Group 1 (4 swine) received intra-arterial and/or intravenous contrast (Conray [iothalamate meglumine] 282 mg/mL; Mallinckrodt, St. Louis, Mo), as part of a separate but concurrent study to evaluate liver and/or kidney imaging, before intracranial hematoma creation. The animals received 660 $\pm$ 85 mL of contrast during 320 $\pm$ 69 minutes, with an additional time interval of 105 $\pm$ 26 minutes between the last injection and the withdrawal of blood for the hematoma creation. The swine in group 1 were representative of patients who develop hematoma during an intervention, after contrast has been administered. Group 2 (3 swine) did not receive contrast medium before hematoma creation. The swine in group 2 were representative of patients who might be evaluated by using C-arm CT before contrast has been administered.

A 1-cm burr hole was created on 1 or both sides of the frontal bone with a surgical perforator. Then a 20 gauge 1.25-inch intravenous catheter (Kendall Healthcare Products, Mansfield, Mass) was introduced into each frontal/parietal lobe through the burr holes to a depth of approximately 2.5 cm from the dura mater. The tip was placed as far away from the skull base as possible to minimize imaging artifact. Proper positioning of the catheter tip was confirmed by rotational imaging before injecting the blood specimen.

A 10-mL blood sample was drawn from the femoral artery line. The hematocrit and activated clotting time were measured. Various volumes of these autologous blood samples were manually injected into the brain parenchyma through the intravenous catheter as summarized in Tables 1 and 2. Each injection was done for 15 minutes to prevent diffusion of blood sample into the subarachnoid space through the needle tract. Animals were first imaged 5 minutes following the completion of the injection (20 minutes after the start of the injection) and then again at 20 minutes in group 1. In group 2, the animals were imaged at 5 minutes after the injection, followed by imaging 20 and 60 minutes later. In 4 animals, a second injection was performed on the opposite side 1 hour later and was also imaged at the same times.

All animals were euthanized after image acquisition with an intravenous injection of beuthanasia solution. The brain of each pig was harvested for pathologic evaluation within 24 hours following the end of each study and was immersed in formalin for fixation for 2 weeks. Then these brains were sliced into 4-mm thicknesses to observe and measure the hematomas.

One additional animal (swine 8) underwent evaluation to verify the renal clearance rates of iodinated contrast in this animal model and to provide an estimate of the iodine concentration in the autologous blood sample injected into the group 1 animals. Residual iodine in the autologous blood sample leads to increased x-ray attenuation of the created intracranial hematoma and, therefore, increased signal intensity in the hematoma relative to background in the reconstructed C-arm CT volume. An estimate of the residual iodine concentration in the circulatory system, and thus in the injected blood, demonstrates the extent to which residual iodine contributes to lesion visibility. Four injections of intravenous contrast of 160 mL each (total 640 mL) were performed into animal 8 at 0, 120, 125, and 130 minutes. Venous blood samples were withdrawn at baseline (ie, before iodine injection) and at 1, 60, 131, and 174 minutes; and 10 mL of

each blood sample was injected into labeled standard "lavender-top" tubes (Monoject; Tyco Healthcare Group, Mansfied, Mass) containing ~0.4 mL of the anticoagulant tri-potassium ethylene-diamine-tetra-acetic acid. C-arm CT images were then acquired of the blood-filled tubes, with additional tubes of water and air and 3 tubes containing 20%, 25%, and 50% contrast in the FOV for calibration purposes. The Hounsfield unit (HU) values in each tube were measured over a 50 × 50 voxel region of interest and were analyzed to determine the Hounsfield unit/([milligram/milliliter] iodine) relationship, as well as the iodine concentration as a function of time after injection of iodine, by using the double exponential decay model described by Hackstein et al[3] given by

$$C(t) = A \cdot e^{-t \cdot B} + C \cdot e^{-t \cdot D} \quad (1)$$

where $C(t)$ equals the iodine concentration in milligrams/milliliter at time t (minutes). The parameters A–D can be determined by using the plasma concentration measurements from the lavender tube samples in conjunction with an assumption about the overall plasma clearance rate. The plasma clearance of the iodinated contrast is calculated as follows:

$$PC[mL/min] = \frac{Q[mg]}{\int_0^\infty C(t)[mg/mL]dt} \quad (2)$$

where the amount of injected iodine Q is known from the injected volume and the iodine concentration of the contrast media.

Image Acquisition

Projection images were acquired by using a state-of-the-art flat panel angiography C-arm system with 30 × 40 cm FPD. Acquisition protocols requiring up to 20 seconds were used for data acquisition, which is the same protocol used in the clinical setting. This protocol provides up to 538 projections along a partial-circle scan C-arm rotation over at least 200°, with the large-area detector providing the ability to image the whole brain in a single sweep. For optimal detector performance, the system relies on an exposure-control system in which a particular detector entrance dose is held constant during the scanning. This is achieved by adjusting the x-ray tube current times product (milliampere-seconds [mAs]) and, if necessary, increasing the tube voltage when a generator (mAs) limit is reached. In summary, the standard acquisition protocol for the C-arm CT system was 538 projections, for 20 seconds, at 74 kV, 230 mA, and 12.5 ms/projection. Double the dose was applied for animal 5, and higher kilovolt (peak) (kVp) values (81 kVp and 109 kVp) were used in animals 6 and 7 in an effort to reduce beam-hardening artifact and to allow more direct comparison with the clinical CT images (see below for discussion of artifact and doses).

Cross-sectional images were reconstructed on an X-Leonardo workstation (Siemens Medical Solutions) by using 3D reconstruction software (DynaCT; Siemens Medical Solutions). The resulting 3D datasets had default isotropic voxel sizes of either 0.2 or 0.4 mm (ie, in-plane resolution of the images was the same as the section thickness), by using a 512 × 512 matrix, and covered up to 18 cm in the cranial-caudal direction. To improve lesion visibility, we averaged neighboring sections to approximately 4 mm for display and analysis by using a "thick MPR" display mode. This increases the effective section width, reduces noise, and is the same as the necropsy section thickness.

Two animals in group 2 were also scanned with clinical conventional CT (Siemens Sensation 16/64, Siemens Medical Solutions) on the same day after C-arm CT acquisition to allow comparison of the image quality with a clinical standard. The imaging protocol used for these studies was a clinical standard and covered the full head and neck of the animal: 100 kV; 300 mAs; reconstructed by using a 512 × 512 matrix; section thickness, 0.75 mm; 366 sections covering a total of 27.5 cm in the cranial-caudal direction.

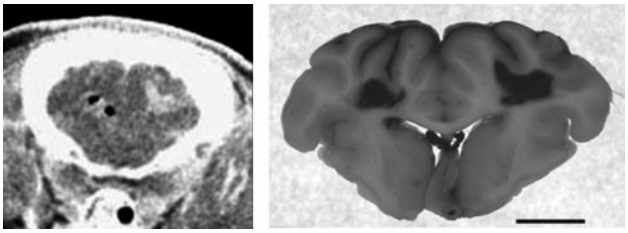

Fig 1. A DynaCT image of group 1 pig brain (left) shows a prominent high-attenuation mass in brain parenchyma on both sides. Necropsied brain of the same pig (right) confirms the intracranial hematomas in the corresponding area and shape. Air was resorbed in the interval between imaging and necropsy. The bar on the right side bottom indicates 10 mm.

Image Analysis

Coronal reconstructions of the last scanning time of each brain (ie, 20-minute postinjection scanning for group 1 and 60-minute postinjection scanning for group 2) were reviewed by a neuroradiologist, and the single section in which the hematoma was most prominent was selected. Acquired data from both C-arm CT and conventional CT were imported into a Macintosh computer using PACS DICOM 3D workstation software (Osirix, free software downloaded from Website http://www.osirix-viewer.com). The section from the multiplanar CT reconstructions corresponding to the section of harvested brain with the hematoma was selected for comparison.

The software ImageJ (National Institutes of Health download: http://rsb.info.nih.gov/ij/) was used to analyze all image data in this study. CT images and scanned images of the harvested brain of each pig were imported into ImageJ. All images were polarized to outline the hematoma margin, and then the area of hematoma was measured. Area measurements of hematoma were compared between C-arm CT and both harvested brain and conventional CT. Percentage difference was calculated by using the following formula:

$$\frac{\text{Area from C-arm CT} - \text{Area from Necropsy)}}{\text{Area from Necropsy}} \quad (3)$$

When a hematoma was not visualized, image analysis was not carried out.

Results

A total of 5 hematomas were created in 4 pigs in group 1. The hematomas ranged from 0.14 to 0.79 cm^2 as measured on the C-arm CT images, and all could be detected with C-arm CT (Fig 1, Table 1). The hematocrits of the blood used to create these hematomas ranged from 19% to 26%. In 1 animal (swine 3), the hematoma ruptured into the lateral ventricle and formed a bilateral intraventricular hematoma (Fig 2). Percentage difference between area measurements from the C-arm CT and harvested brain ranged from 0% to 29.4%, with the difference being larger in small hematomas.

A total of 6 hematomas were created in 3 pigs from group 2. Three of these hematomas were not visualized as a high-attenuation mass (Table 2). One of the nonvisualized hematomas

Fig 2. DynaCT section of pig 3 shows high-attenuation intraventricular hemorrhage casting the lateral ventricles.

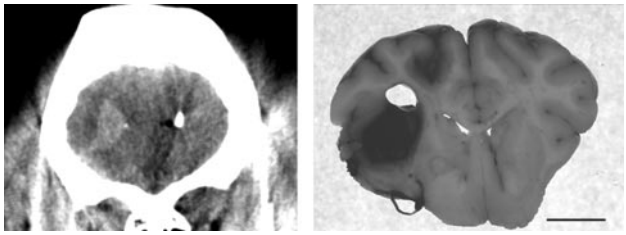

Fig 3. DynaCT image of group 2 pig brain (left) shows a prominent high-attenuation mass in brain parenchyma on the right side. High attenuation in the left brain is the catheter used to create a hematoma; however, no hematoma was seen. Necropsied brain of the same pig (right) confirms the intracranial hematoma in the right brain; no hematoma was confirmed on the left.

could not be confirmed with necropsy (Fig 3). The other 2 hematomas, which could not be detected by using C-arm CT imaging, were created with blood of lower hematocrits (21% and 22%). The 3 hematomas that were visualized with C-arm CT ranged in size from 0.17 to 0.77 cm^2 and were created with blood hematocrits of 29%–37%. Three hematomas from 2 animals in group 2 were scanned with both conventional CT and C-arm CT. All 3 hematomas were detected with both techniques as a high-attenuation mass (Fig 4). The high attenuation was more prominent in the conventional CT image compared with C-arm CT images. However, the shape and size of the hematomas were closely correlated between the 2 techniques. These measurements are shown in Table 3. The percentage difference of area measurement between conventional CT brain and C-arm CT of each hematoma was 7.6%, 14.6%, and 11.4%. It is not known whether the 2 lower hematocrit hematomas not visualized on C-arm CT would have been seen on conventional CT because we did not obtain conventional CT scans for all the animals due to limited access to the clinical scanner.

The hematomas that were visualized in both group 1 and group 2 animals could all be seen immediately (ie, at the earliest time point, 5-minutes postinjection). The conspicuity of these bleeds did seem to improve slightly with time.

The renal clearance results in animal 8 were used to estimate the iodine concentration of the blood in the animals in group 1 as follows: First, the conversion between iodine concentration and Hounsfield unit was calculated by using the known concentrations of iodine and found to be 0.043 mg/mL per Hounsfield unit. The measured iodine concentrations at the 5 time points were the following: baseline = 6 ± 58 HU or ~0 mg/mL; 1 minute = 35 ± 73 HU or 1.50 mg/mL; 60 minutes = 25 ± 30 HU or 1.07 mg/mL; 131 minutes = 278 ± 51 HU or 11.9 mg/mL; and 174 minutes = 161 ± 64 HU or 6.89 mg/mL. Hackstein et al[3] found the renal clearance rate in healthy adults to show significant variability, with a mean of 79.8 mL/min and a range of 33–141 mL/min.

Using a mean clearance rate of 80 mL/min as an additional fit constraint and the previously measured iodine concentrations at 131 and 174 minutes, we found values for the constants A, B, C, and D in equation 1 to be 5.30, 0.039, 6.29, and 0.0028, respectively. Equation 1 with the fitted parameters was then used to provide an estimate of residual contrast concentration following a bolus injection of 660 mL of contrast, with a time interval of 105 minutes between contrast injection and blood withdrawal, and the estimate was found to be 4.77 mg/mL, or 111 HU. This is an upper bound on the attenuation of the blood because the fit parameters were derived by using samples from an injection protocol for which most of the contrast was injected within 10 minutes of the first postcontrast blood draw. The same model can be used to estimate the effect of smaller injections (~150 mL per injection) equally spaced for 320 minutes (ie, at 0 and every ~105 minutes thereafter for a total of 4 injections), a protocol that more closely approximates the experimental scenario in group 1. After 4 injections and with a final interval of 105 minutes after the last injection, the blood iodine signal intensity was estimated to be 3.92 mg/mL, or 91 HU (fit parameters were 0.28, 0.00037, 1.54, and 0.0096 for A, B, C, and D, respectively).

Discussion

The aim of this study was to evaluate the ability of the FPD C-arm CT to detect hemorrhagic lesions within a pig brain by using an intracranial hematoma model. Three major factors contributed to the ability to detect lesions: 1) the presence/absence of iodinated contrast, 2) the hematocrit of the created lesion, and 3) the artifact level in the C-arm CT images.

Creating Realistic ICH in a Swine: Injecting Autologous Blood

In this study, we used a swine model with injection of unclotted autologous blood into brain. Autologous blood infusion may be the most widely used method to create ICH, despite the challenges of the technique and the disadvantages of possible ventricular rupture and backflow of blood along the needle tract. Deinsberger et al[4] modified this method to overcome these disadvantages by using a double-injection technique. Another group placed a balloon catheter and inflated it within the brain to make a cavity before injecting blood.[5-7] We injected the blood sample slowly and continuously through a catheter without creating a cavity in a manner previously described[8] to successfully create 11 ICHs. Some of our ICHs were accompanied by intraventricular and/or subarachnoid hemorrhage (SAH), which was confirmed with necropsy. These probably contributed to the difference in hematoma size between those animals that were injected with the same amount of blood. One infusion could not be seen at necropsy (animal 6). In this case, we found subarachnoid hematoma along the needle tract, which did not perforate into the gray matter. This suggested that the needle placement was not deep enough, and

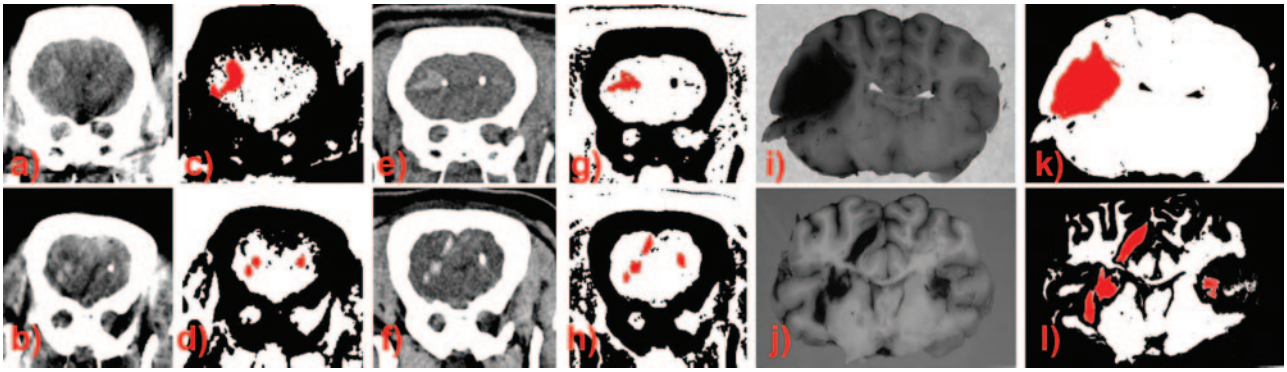

Fig 4. A series of pictures used for area measurement on pigs 6 (*upper row*) and 7 (*lower row*). A coronal section of brain images (*A* and *B*) obtained with the C-arm CT system shows a high-attenuation mass within brain parenchyma. The high-attenuation areas are polarized and digitally selected as a red mass by ImageJ software (*C* and *D*). Coronal sections of brain images obtained with conventional CT (*E* and *F*) show intracranial hematoma as a prominent high-attenuation mass. These high-attenuation areas are measured by ImageJ software after polarization (*G* and *H*). Harvested necropsied brains reveal intracranial hematoma (*I* and *J*). The hematoma areas are measured by ImageJ software with the same technique as used in the measurement of hematoma area of C-arm CT and conventional CT (*K* and *L*).

Table 3: Comparison conventional CT and necropsy hematoma areas

Animal No.	Side	Injected Volume (mL)	Hct (%)	ACT (second)	Area from Conventional CT (cm^2)	Area from Necropsy Brain (cm^2)	Difference (% difference)
6	Rt	5	37	87	1.33	1.43*	0.10 (7.0)
	Lt	5	31	70	Nonvis	N/A	N/A
7	Rt	5	29	146	0.62	0.58	−0.04 (6.9)
	Lt	5	35	59	0.20	0.13	−0.07 (53.8)

Note:—Hct indicates hematocrit; ACT, activated clotting time; Nonvis, nonvisible; Rt, right; Lt, left; N/A, not available.
* Necropsy area measured for animal 6 differs from the value in Table 2 because a different section was used for the comparison between the conventional pathologic specimen and conventional CT.

the infused blood traveled back along the needle tract into the low-resistance subarachnoid space.

The SAH could not be identified by either C-arm or conventional CT but was seen at necropsy. At necropsy, the SAH was diffusely distributed from the convexity to the basal cisterns. Beam-hardening from the small cranial space may have made it difficult to differentiate SAH from artifact.

Creating Realistic ICH in a Swine: Hematocrit

Several factors contribute to the high attenuation of ICH seen on CT images, including size, age, and location of the hematoma,[9] and it is well known that CT attenuation increases linearly in accordance with both hematocrit and hemoglobin concentration.[10,11] An ICH due to blood with a hemoglobin concentration of >9–11 mg/dL (this approximately equals a hematocrit of 28%–35%) is seen as high attenuation on CT.[12] The blood injected into the animals in this study had hematocrits that varied between 19%–35% and were lower than the normal value quoted for humans of approximately 39%, and we therefore expected the inherent contrast of the created lesions to be lower than would be seen in clinical scenarios. We found that a hematocrit of >29% causing a hematoma of 0.58 cm^2 could be detected by C-arm CT in the absence of any contrast medium. On the other hand, similar-sized hematomas (0.41 and 0.46 cm^2) created with hematocrits of 21% and 22% could not be seen by C-arm CT. An exact lower level for hematocrit detection cannot be given here because we did not evaluate image quality for hematomas created with blood having hematocrits between 22% and 29% in the group 2 animals. However, C-arm CT appears to be similar to conventional CT in its ability to detect hematomas on the basis of size and for the hematocrits we did evaluate.

Creating Realistic ICH in a Swine: Presence of Iodinated Contrast

The attenuation of acute hemorrhage as seen on clinical CT is ~80 HU,[13] whereas extravasated contrast material following a CT angiography examination (indicating an active bleed) has higher values of 150–350 HU,[14] for which a typical contrast injection is 100 mL of 300 mg/mL iodinated contrast. We estimate the attenuation of the iodinated blood used in the group 1 animals to be ~90–110 HU, slightly higher than acute hemorrhage alone but lower than that seen following CT angiography. However, a weakness of this study is that we do not know the precise effect of the contrast on attenuation in the individual animals. The group 1 animals, therefore, represent a clinical scenario where an interventional procedure is underway and some iodinated contrast has been injected, an intracranial hemorrhage is suspected with extravasation of some contrast material, and C-arm CT can then be used for immediate detection or exclusion of intracranial complication without patient transfer. This clinical scenario has recently been described by Heran et al[2] in a case study in which the quality of C-arm CT was found to be sufficient for diagnosis.

Imaging ICH: Image Quality with C-arm CT

Conventional CT confirmed the findings of C-arm CT in 2 swine in group 2. However, hematomas were more prominent and better defined with conventional CT compared with C-arm CT. The difference in image quality indicates that the low-contrast resolution of the FPD is not yet equivalent to that of clinical CT, and further improvements are necessary.

In clinical CT, scatter and beam-hardening artifacts affect image quality,[15] and because C-arm CT is based on identical physical principles, it is affected by the same artifacts. How-

ever, design trade-offs that allow 2D and 3D imaging with the same system, including detectors sized for area projection imaging (larger in the axial direction than clinical CT, but not as wide as clinical CT detectors); detectors with high spatial resolution; and a mechanical C-arm gantry that provides oblique angle flexibility lead to increased artifact in C-arm CT images.

Limited detector width may produce artifact due to truncation if an object extends beyond the detector width in some (or even all) x-ray projections, though the 40-cm detector used here is usually wide enough to cover a normal skull when the patient is properly isocentered, so this was not a source of error in this study. Conversely, the extent of the detector in the axial direction causes a significantly higher contribution from scattered radiation than projections acquired on a clinical CT scanner due to a significant increase in simultaneously irradiated volume. Scattered radiation reduces the quality of the reconstructed image through cupping, streaks, a decrease in contrast, and additional noise,[16-18] causing cupping, shadowing, and streak artifacts. Although scatter can be reduced by using narrow collimation, this may not be clinically practical if the location of the lesion is not known a priori. The correction approach implemented here estimates the primary radiation from the projection data by using an iterative method involving a multiplicative correction step,[19] and further improvements by using iterative techniques, hardware approaches, or a combination of the 2 are possible.[20-30]

The number of views taken over a partial-circle scan can also be a limiting factor for image quality if insufficient angular sampling (ie, too large an angle between views) occurs. The Feldkamp reconstruction algorithm[31] with a generalized Parker weighting scheme,[32] acquiring projections over at least 180° plus the fan angle of the x-ray beam, with 538 views spaced 0.4° apart, provided images that were free of view aliasing on the midplane. Unfortunately, a single partial-circle (or even full circle) scan in the cone-beam geometry provides inherently incomplete data for reconstructing sections off the midplane of the acquired volume, leading to streaking and shading that increases in severity as the plane of interest moves away from the midplane of the acquisition.[33-37] Note, however, that the brain of the swine is relatively small in the z-direction, so evidence of cone-beam artifact was not seen in this study.

Beam-hardening was likely a significant source of streak artifact, occurring primarily between attenuated objects and at sharp edges in the swine images. Large-area detectors used for angiographic procedures are optimized to operate at 80–90 kVp to highlight the presence of iodine[38] as compared with 120 kVp for clinical CT. The correction method used here applies a polynomial operation to restore a linear relationship between projection value and path length, assuming water-equivalent object conditions.[20] Although this software-based method reduces cupping effectively, it cannot completely remove the streaking and shading artifacts and other more sophisticated beam-hardening correction methods (eg, based on iterative modifications of x-ray projection images as described in Hsieh et al[39]) could be used to further improve image quality.

A final artifact that can appear in CT images is rings, caused by residual detector-gain inhomogeneities that remain after detector flat-field calibration; our artifact-correction algorithm (extract a ring artifact image from each reconstructed C-arm CT section, then subtract that image from the original section)[19] is effective, and no evidence of this artifact was seen in our swine images.

In summary, we estimate that the significant image artifact in the C-arm CT images was due primarily to scatter and beam-hardening. However, despite the presence of such artifact, the shape of the hematomas was well correlated between images from C-arm CT and conventional CT; and for higher hematocrits or with some iodine on board, image quality was clearly adequate to detect the hematomas.

Imaging ICH: Dose with C-arm CT

During our studies, we primarily relied on 20-second acquisition protocols with the x-ray source voltage usually set at (nominal) 70 kVp. There were 2 exceptions in which we imaged at 81 kVp (animal 6) and 109 kVp (animal 7) to reduce beam-hardening artifacts by increasing the number of higher energy x-ray photons relative to their lower energy counterparts. Using conversion factors measured by Fahrig et al[38] for the same system and assuming a 70-kVp beam, the dose for the standard C-arm CT protocol used here corresponds to weighted dose values of approximately 70 mGy. The recommended dose for routine clinical head CT scans is 60 mGy,[40] indicating that adequate image quality for lesion detection can be achieved at a dose that is only slightly higher than that used for clinical CT scanning. In animal 5 (group 2), C-arm CT could not detect the hematoma even with the high-weighted dose value of 131 mGy, which is more than double that of standard head CT scanning; though because a corresponding clinical scan was not obtained for that animal, it is not known whether the hematoma would have been visualized by using clinical CT. Note that though increased scatter-detection degrades C-arm CT image quality relative to clinical CT (as described previously), the total x-ray scatter produced during a scanning of the head is the same for both techniques if the same volume is imaged, so there is not an increase in patient dose due to the scatter environment.

Image Quality: Accuracy of the Size of Hematomas

The limiting spatial resolution of C-arm CT is reported to be 0.20 mm and is generally not considered to be a limiting feature of the system because it exceeds that of clinical CT. In this study, C-arm CT could detect the hematoma size of as small as 0.14 cm^2 in group 1 and 0.13 cm^2 in group 2. The percentage difference between the sizes measured from the C-arm CT image and necropsy of the brain ranged from 1.0% to 34.5%. Although we could not perform statistical evaluation due to the small number of subjects, larger hematomas tend to show smaller percentage differences between the measurements. This is likely due to the measurement method. Before measurement, the image underwent polarization, which is crucial to measuring the area with ImageJ. This procedure automatically decides whether a pixel is white or black. Around the edges of hematoma, some pixels may be interpolated into black (hematoma) and others into white (not hematoma). This automatic process might introduce error. Because the pixel size of the images of both large and small hematomas is the same, a small hematoma will be more affected by this error.

Limitations of the Study

There are some limitations to this study. The small number of hematomas created does not allow a more clearly defined lower

limit to lesion detection based on size or hematocrit. However, the study was able to show that small hematomas with hematocrits of approximately 30% were detectable with C-arm CT.

Another limitation of this study is that a slightly higher weighted dose was used for the image acquisition than is usually recommended for routine CT scanning. The swine model has a smaller intracranial space and brain than that of humans, which restricted the injection volume of autologous blood. The smaller intracranial space also increases beam-hardening artifacts from both bony structures of the skull base and from the surgically drilled burr holes, making the imaging task significantly more challenging than in a clinical setting and reducing the detection of smaller hematomas. This was further affected by having to image in a coronal plane, which causes the beam to traverse the skull base. A higher weighted dose was, therefore, chosen in an effort to overcome the increased artifact and to ensure that x-ray quantum noise did not limit the detection of the lesions (Fig 3).

A final limitation of the study is that it did not include a group with heparinized blood. Heparin would prevent fibrin mesh formation, which leads to clot retraction. This may lead to the creation of fluid-blood levels in the acute ICH. Backflow along the needle tract would need to be prevented to create such a hematoma cavity in an animal model. A model using a balloon catheter to create a hematoma cavity might overcome this difficulty.[5-7]

Conclusion

The aim of this study was to evaluate the ability of the FPD C-arm CT to detect small intracranial hematomas in a swine brain model. C-arm CT was able to detect small (<1.0 cm^2) experimentally created intracranial hematomas with hematocrits in the range of 29%–35%. When intravascular contrast was administered, all hematomas could be detected in the C-arm CT images even when the hematocrit was 19%–20%. The results of the present study support the hypothesis that this imaging technique could be used for the recognition and management of complications of interventional neuroradiology procedures. Further work needs to be performed to demonstrate the efficacy of C-arm CT in the evaluation of intracranial hemorrhage in a clinical neurointerventional setting.

Acknowledgments

We thank Diane Howard, DVM, and Wendy Baumgardner, DVM, for animal care during the procedures, Jerry Kneebone and Maria Lozada-Parks for assistance with clinical CT image acquisition, and F. Graham Sommer, MD, for technical assistance.

References

1. Benndorf G, Strother CM, Claus B, et al. **Angiographic CT in cerebrovascular stenting.** *AJNR Am J Neuroradiol* 2005;26:1813–18
2. Heran NS, Song JK, Namba K, et al. **The utility of DynaCT in neuroendovascular procedures.** *AJNR Am J Neuroradiol* 2006;27:330–32
3. Hackstein N, Cengiz H, Rau WS. **Contrast media clearance in a single kidney measured on multiphasic helical CT: results in 50 patients without acute renal disorder.** *AJR Am J Roentgenol* 2002;178:111–18
4. Deinsberger W, Vogel J, Kuschinsky W, et al. **Experimental intracerebral hemorrhage: description of a double injection model in rats.** *Neurol Res* 1996;18:475–77
5. Kuker W, Thiex R, Rohde I, et al. **Experimental acute intracerebral hemorrhage: value of MR sequences for a safe diagnosis at 1.5 and 0.5 T.** *Acta Radiol* 2000;41:544–52
6. Rohde V, Rohde I, Thiex R, et al. **Fibrinolysis therapy achieved with tissue plasminogen activator and aspiration of the liquefied clot after experimental intracerebral hemorrhage: rapid reduction in hematoma volume but intensification of delayed edema formation.** *J Neurosurg* 2002;97:954–62
7. Rohde V, Rohde I, Thiex R, et al. **The role of intraoperative magnetic resonance imaging for the detection of hemorrhagic complications during surgery for intracerebral lesions: an experimental approach**. *Surg Neurol* 2001;56:266–74, discussion 274–75
8. Wagner KR, Xi G, Hua Y, et al. **Lobar intracerebral hemorrhage model in pigs: rapid edema development in perihematomal white matter.** *Stroke* 1996;27:490–97
9. Cohen W, Hayman L. **Computed tomography of intracranial hemorrhage.** *Neuroimaging Clin N Am* 1992;2:75–87
10. New PF, Aronow S. **Attenuation measurements of whole blood and blood fractions in computed tomography.** *Radiology* 1976;121:635–40
11. Norman D, PriceD, Boyd D, et al. **Quantitative aspects of computed tomography of the blood and cerebrospinal fluid.** *Radiology* 1977;123:335–38
12. Taber K, Hayman L, Diaz-Marchan P. **Intracranial hemorrhage.** In: Orrison W Jr, ed. *Neuroimaging*. Vol. 1, Philadelphia: Saunders; 2000:853–83
13. Sanelli PC, Mifsud MJ, Zelenko N. **CT angiography in the evaluation of cerebrovascular diseases.** *AJR Am J Roentgenol* 2005;184:305–12
14. Holodny AI, Farkas J, Schlenk R, et al. **Demonstration of an actively bleeding aneurysm by CT angiography.** *AJNR Am J Neuroradiol* 2003;24:962–64
15. Gupta R, Jones ES, Mooyaart EA, et al. **Computed tomographic angiography in stroke imaging: fundamental principles, pathologic findings, and common pitfalls.** *Semin Ultrasound CT MR* 2006;27:221–42
16. Fox TR, Nisius DT, Aradate H, et al. **Practical x-ray scatter measurements for volume CT detector design.** *Proceedings of SPIE* 2001;4320:808–14
17. Siewerdsen JH, Jaffray DA. **Cone-beam computed tomography with a flat-panel imager: magnitude and effects of x-ray scatter.** *Med Phys* 2001;28:220–31
18. Endo M, Mori S, Tsunoo T, et al. **Magnitude and effects of x-ray scatter in a 256-slice CT scanner.** *Med Phys* 2006;33:3359–68
19. Zellerhoff M, Scholz B, Ruehrnschopf EP, et al. **Low contrast 3D reconstruction from C-arm data.** Proceedings of SPIE, 2005;5747:646-55
20. Zhu L, Bennett NR, Fahrig R. **Scatter correction method for x-ray CT using primary modulation: theory and preliminary results.** *IEEE Trans Med Imaging* 2006;25:1573–87
21. Siewerdsen JH, Moseley DJ, Bakhtiar B, et al. **The influence of antiscatter grids on soft-tissue detectability in cone-beam computed tomography with flat-panel detectors.** *Med Phys* 2004;31:3506–20
22. Siewerdsen JH, Jaffray DA. **Optimization of x-ray imaging geometry (with specific application to flat-panel cone-beam computed tomography).** *Med Phys* 2000;27:1903–14
23. Wiegert J, Bertram M, Schafer D, et al. **Performance of standard fluoroscopy anti-scatter grids in flat-detector-based cone-beam CT.** *Proceedings of SPIE* 2004;5368:67–78
24. Ning R, Tang X, Conover D. **X-ray scatter correction algorithm for cone beam CT imaging.** *Med Phys* 2004;31:1195–202
25. Seibert JA, Boone JM. **X-ray scatter removal by deconvolution.** *Med Phys* 1988;15:567–75
26. Seibert JA, Boone JM. **Medical image scatter suppression by inverse filtering.** *Proceedings of SPIE* 1988;914:742
27. Spies L, Ebert M, Groh BA, et al. **Correction of scatter in megavoltage cone-beam CT.** *Phys Med Biol* 2001;46:821–33
28. Bertram M, Wiegert J, Rose G. **Potential of software-based scatter corrections in cone-beam volume CT: progress in biomedical optics and imaging.** *Proceedings of SPIE* 2005;5745:259–270
29. Wiegert J, Bertram M, Rose G, et al. **Model-based scatter correction for cone-beam computed tomography: progress in biomedical optics and imaging**. *Proceedings of SPIE* 2005;5745:271–282
30. Kruger DG, Zink F, Peppler WW, et al. **A regional convolution kernel algorithm for scatter correction in dual-energy images: comparison to single-kernel algorithms.** *Med Phys* 1994;21:175–84
31. Feldkamp LA, Davis LC, Kress JW. **Practical cone-beam algorithm.** *Journal of the Optical Society of America A* 1984;1:612–19
32. Parker DL. **Optimal short scan convolution reconstruction for fanbeam CT.** *Med Phys* 1982;9:254–57
33. Lee SW, Wang G. **A Grangeat-type half-scan algorithm for cone-beam CT.** *Med Phys* 2003;30:689–700
34. Noo F, Heuscher D. **Image reconstruction from cone-beam data on a circular short-scan.** *Proceedings of SPIE* 2002;4684:50–59
35. Defrise M, Clack R. **A cone-beam reconstruction algorithm using shift-variant filtering and cone-beam backprojection.** *IEEE Trans Med Imaging* 1994;13:186–95
36. Nett B, Zhuang T-L, Leng S, et al. **Arc-based cone-beam reconstruction algorithms using an equal weighting scheme.** *J X-ray Sci Technol* 2007;15:19–48
37. Grass M, Kohler T, Proksa R. **3D cone-beam CT reconstruction for circular trajectories.** *Phys Med Biol* 2000;45:329–47
38. Fahrig R, Dixon R, Payne T, et al. **Dose and image quality for a cone-beam C-arm CT system.** *Med Phys* 2006;33:4541–50
39. Hsieh J, Molthen RC, Dawson CA, et al. **An iterative approach to the beam hardening correction in cone beam CT.** *Med Phys* 2000;27: 23–29
40. Gray JE, Archer BR, Butler PF, et al. **Reference values for diagnostic radiology: application and impact.** *Radiology* 2000;235:354–58